Effect of Free-Stream Turbulence on the Hydrodynamic Performance and Wake Structure of an H-Darrieus Tidal Turbine

By

Chad Magas
B. Eng., University of Victoria, 2021

A Thesis Submitted in Partial Fulfillment
of the Requirements for the Degree of

MASTER OF APPLIED SCIENCE

in the Department of Mechanical Engineering

We acknowledge and respect the Lək̓ʷəŋən (Songhees and Xʷsepsəm/Esquimalt) Peoples on whose territory the university stands, and the Lək̓ʷəŋən and W̱SÁNEĆ Peoples whose historical relationships with the land continue to this day.

Effect of Free-Stream Turbulence on the Hydrodynamic Performance

and Wake Structure of an H-Darrieus Tidal Turbine

By

Chad Magas

B. Eng, University of Victoria, 2021

Supervisory Committee

Dr. Peter Oshkai, Supervisor

(Department of Mechanical Engineering)

Dr. Brad Buckham, Department Member

(Department of Mechanical Engineering)

Abstract

An increasing awareness of the impact of anthropogenic pollution on climate and ecosystems has driven innovation and research into renewable energy technologies. Hydrokinetic energy harvesting of tidal events is among the most promising of these renewable technologies due to the predictability of tides. The H-Darrieus turbine stands out as one of the most capable devices for this energy conversion. Despite continued research efforts, the effects of free-stream turbulence on H-Darrieus turbines still pose substantial challenges in both the research and implementation of these devices.

The present work investigates the effect of free-stream turbulence on the hydrodynamic performance and wake structure of an H-Darrieus tidal turbine. To perform this investigation, experiments were conducted in the recirculating water channel inside the University of Victoria's Fluid Mechanics Laboratory. The turbine used was a 1/10th scale H-Darrieus turbine, operating at the diameter-based Reynolds number 0.5×10^6. Fractal grids were installed upstream of the turbine to generate three distinct free-stream inflow turbulence levels: 1.4% (baseline), 4.7% (intermediate), and 10.4% (high). The performance of the turbine was evaluated at each turbulent interval across the tip-speed ratio (TSR) range of $1.0 \leq \mathrm{TSR} \leq 3.4$. Quantifying the performance was achieved through continuous measurement of the shaft torque and azimuthal position data. The wake structure of the turbine was characterised at TSR = 2.65 using particle image velocimetry to obtain ensemble- and phase-averaged velocity measurements.

Phase-resolved performance data suggest that an increase in free-stream turbulence delays the onset of stall and accelerates the reattachment of the boundary layer, impacting critical azimuthal angles at which the turbine rotor interacts with the free-stream. These results demonstrate an increase in quasi-periodicity of shaft torque with increasing free-stream turbulence, leading to greater cycle-to-cycle azimuthal variance in vortex shedding.

The wake flow fields obtained at TSR = 2.65 indicate that elevated levels of free-stream turbulence decrease the transition distance from near- to far-wake. This decrease in wake coherence is a result of increased quasi-periodicity in the vortex shedding. Furthermore, increased free-stream turbulence was found to increase the streamwise velocity deficit, leading

to a delayed wake recovery. This decrease in the total streamwise momentum recovery is suggested to be the cause of a reduction in the out-of-plane transportation, representing a faster breakdown and dissipation of blade tip-vortices.

These results offer direct implications in the context of tidal turbine design and deployment. The increase in quasi-periodicity of the turbine with elevated turbulence introduces non-periodic loading as well as a decreased unloading period onto the turbine blades. This increase in load and decrease in loading time may require a more robust turbine design and system integration strategy, depending on the free-stream turbulence characteristics of the tidal environment. Additionally, the change in momentum transfer rate in the wake of the turbine will require additional consideration for optimal turbine array spacing.

Table of Contents

List of Tables

List of Figures

Nomenclature

List of Symbols

α	Angle of Attack [°]
α_{eff}	Effective Angle-of-Attack [°]
$A_{Proj.}$	Projected Area $[m^2]$
β	Blade Pitch Angle [°]
c	Chord Length of the Blade $[m]$
C_p	Power Coefficient $[-]$
D	Turbine Diameter $[m]$
l	Integral Length Scale $[m]$
r	Turbine Radius $[m]$
Re_d	Diameter-Based Reynolds Number $[-]$
Re_c	Chord-Based Reynolds Number $[-]$
Re_λ	Taylor-Based Reynolds Number $[-]$
U_{eff}	Effective Flow Velocity $[m/s]$
U_∞	Free-Stream Velocity $[m/s]$
$\boldsymbol{U}(U,V,W)$	Local Velocity $[m/s]$
$\boldsymbol{X}(X,Y,Z)$	Spatial Coordinates $[m]$
θ	Rotor Azimuthal Angle [°]
λ	Taylor Microscale Length $[m]$
ϵ	Dissipation Rate of Turbulent Kinetic Energy $[m^2/s^2]$

η	Kolmogorov Dissipation Scale $[m]$
ρ	Fluid Density $[kg/m^3]$
τ	Torque $[Nm]$
ν	Kinematic Viscosity $[m^2/s]$
ω	Angular Velocity $[rad/s]$

Abbreviations

2D	Two-Dimensional
3D	Three-Dimensional
CFD	Computational Fluid Dynamics
LEV	Leading Edge Vortex
PIV	Particle Image Velocimetry
TEV	Trailing Edge Vortex
TI	Turbulence Intensity
TSR	Tip Speed Ratio

Acknowledgments

I want to express my sincere gratitude to:

Dr. Peter Oshkai, my supervisor, for his guidance, support, encouragement, and patience, all of which have fostered growth beyond the work presented in this thesis;

Dr. Artem Korobenko, whose passion for renewable energy laid the foundation for this work;

My research groupmates: Duncan McIntyre, Sierra Mann, Curtis Evans, Zackary Baycroft, and Ben Raddysh, for their consistent support throughout this process;

My mother, Chris Christiansen, for her continuous support and belief in my academic journey;

And my partner, Elora Koster, for her sustained support during both the productive and difficult stretches.

Chapter 1: Introduction

1.1 Background and Motivations

The global dependence on energy is undisputable and continues to grow with each successive year, averaging an annual growth in demand of 2.25% [1]. The rise in awareness of global warming has highlighted our reliance on fossil fuels, which are the largest source of energy consumed, accounting for a staggering 82% of the global energy consumption in 2023 [2]. Our fossil fuel dependency is also the most significant contributor to climate change, accounting for 75% of global anthropogenic greenhouse gas emissions and 90% of all carbon dioxide emissions [3], which is the leading cause of human-induced global warming [4]. Although the impact of these anthropogenic emissions has been known since the introduction of the carbon dioxide theory of climate change in 1955 [5], it was not until the past decade that an effort to address our dependency on fossil fuels was made, primarily through the Paris Agreement. Although the efficacy of this agreement is still debated, many participating countries have actively made efforts to research, develop, and implement renewable energy devices to harvest wind, solar, and hydrokinetic energy [6], [7], [8]. The goal of diversifying into renewable energy is to help alleviate dependence on fossil fuels and grow with the annual increase in energy demand.

Among the three most promising renewable energy technologies: wind, solar, and hydrokinetic, hydrokinetic turbines located in streams, rivers, and tidal sites offer the most predictable and consistent energy conversion [9]. With hydrokinetic turbines, there are two dominant styles, characterised by the axis of rotation. The two types are axial-flow and cross-flow turbines [10], depicted in Figure 1.1, where the most common cross-flow turbine design is the H-Darrieus turbine. This style of cross-flow turbine is defined by its straight blades mounted parallel to the axis of rotation. The blades are connected to the turbine's shaft by supporting struts, forming an "H"-shaped rotor. Although the H-Darrieus cross-flow turbine has gained interest over the years, axial-flow turbines are the more established styles, with the axis of rotation being ideally parallel to the incoming free-stream flow. These turbines are designed with a yawing mechanism to ensure the optimal positioning of the turbine with respect to the flow. Cross-flow

turbines, on the other hand, operate with the axis of rotation perpendicular to the incoming flow, leading to a turbine that is optimally positioned regardless of the inflow direction.

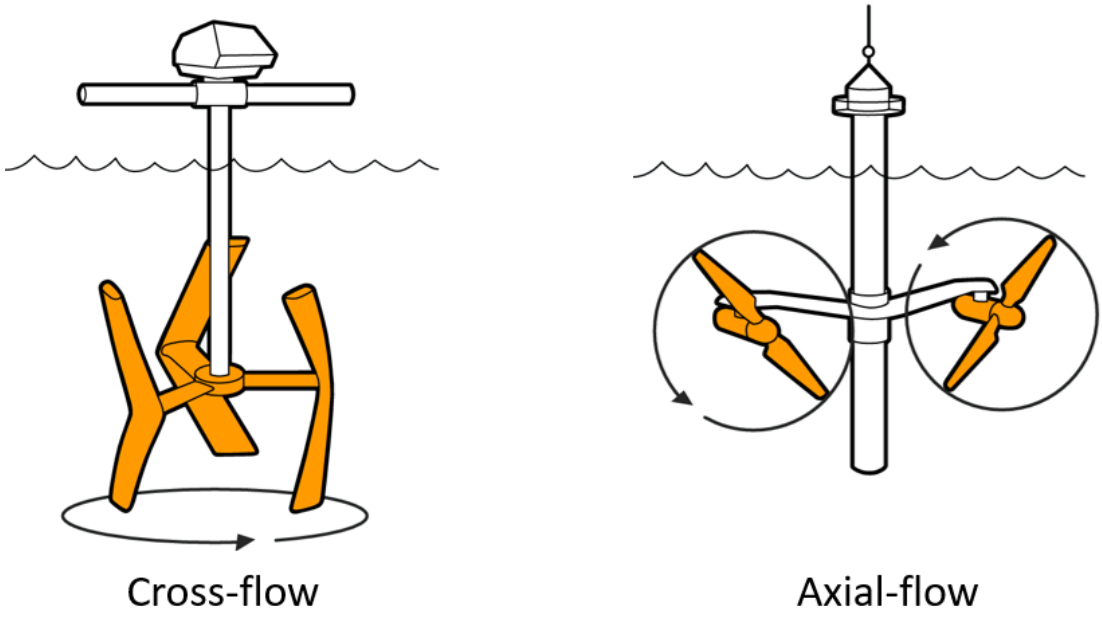

Figure 1.1: Depictions of a Cross-flow turbine (left) and an axial-flow turbine (right). Modified from Hydro-Québec [11].

Another difference between cross- and axial-flow turbine designs is the electrical generator placement. With the generators being affixed to the rotor, axial-flow turbine generators are therefore underwater, requiring additional costs for manufacturing and servicing waterproof enclosures. Cross-flow turbines place the generator above the water's surface, evading these additional costs [12]. Cross-flow turbines also offer a rectangular power extraction window, opposed to the circular extraction window inherent to the axial-flow turbine design [13]. This difference leads to two main advantages. Firstly, cross-flow turbines have a larger power extraction window than axial flow, and secondly, cross-flow turbines can be installed in places that axial-flow turbines cannot simply by adjusting the aspect ratio of the rotor. Some of the additional installation locations include dam raceways and shallow rivers or streams [14] [15]. One of the last major differences in the design is the turbine blades. Cross-flow turbines typically employ blades with a uniform profile along the entire span, whereas axial-flow turbines have a

continually varying pitch and chord lengths along the span of the blade. This difference has the potential to reduce manufacturing costs and time in cross-flow turbines.

Despite a strong list of advantages, an incomplete understanding of the impact of real-world operating conditions on cross-flow turbines impedes the ability to accurately predict power extraction performance and wake characteristics of these devices. Unlike controlled laboratory environments or idealized numerical simulations, turbulence presented in tidal, stream, and river installation sites influences these turbines in undesirable ways [16]. Some of the more notable impacts include blade loading and increased fatigue, which can lead to premature failures [17]. Developing a deeper understanding of the impact of turbulence on cross-flow turbines performance and wake structure will support and improve the optimization of geometry, inter-device spacing, grid integration, fatigue management, and more precise estimations of power output expectations.

1.2 Thesis Structure

The main body of this thesis consists of a single chapter, written in the form of an independent manuscript with the intent of submission to a peer-reviewed journal. Modifications to the manuscript's headings, figures, tables, plots, and reference numberings, alongside reference stylings, have been made to maintain consistency with this document. The thesis is closed with an inclusive summary of the findings and recommendations for future work.

Chapter 1

This chapter Introduces the motivation for research and development of renewable energy technologies and presents general background information on the cross-flow turbine. The background information includes the advantages and disadvantages when compared to other promising renewable technologies and the advantages of other leading turbine designs. The chapter concludes with a brief remark on motivation and objectives for the present thesis.

Chapter 2

Magas, C., Oshkai, P., Korobenko, A. (2025). “Effect of Free-Stream Turbulence on the Power Extraction Performance and Wake Structure of a Cross-flow Turbine.” In preparation for submission to the *Journal of Renewable Energy*.

This chapter consists of a manuscript prepared by the present thesis author. This manuscript reviews the current literature on the topic of turbulent effects on the performance and wake of cross-flow turbines, introduces the experimental setup, and then presents the results and discussion. The experimental design, setup, data acquisition, and processing were all performed by the author of the present thesis. The original draft was also written by the present author, with Dr. Oshkai providing guidance and research direction, as well as editing the manuscript. Dr. Korobenko is responsible for providing final revisions and was the one who initiated the project topic.

Chapter 3

The final chapter presents a restatement of the principal conclusions derived from the presented research and concludes by providing several recommendations for future work.

Chapter 2: Effect of Free-Stream Turbulence on the Power Extraction Performance and Wake Structure of a Cross-flow Turbine

Chad Magas [a], Peter Oshkai [a], Artem Korobenko [b]

[a] Department of Mechanical Engineering, University of Victoria

[b] Department of Mechanical Engineering, University of Calgary

2.1 Abstract

The effect of free-stream turbulence on a 1/10th scale H-Darrieus tidal turbine was investigated through a series of experiments conducted in a water tunnel at the diameter-based Reynolds number 0.5×10^6. The inflow turbulence level was varied between 1.4%, 4.7%, and 10.4% by the installation of fractal grids upstream of the test section. The performance of the turbine was characterized across a broad range of tip-speed ratios from 1.0 to 3.4 using continuous measurements of the torque applied to the shaft of the turbine rotor. Particle image velocimetry was employed to obtain ensemble- and phase-averaged velocity measurements in the wake of the turbine at the tip-speed ratio of 2.65 for each turbulent interval.

The phase-resolved performance data revealed that, aside from increasing the quasi-periodic response of torque, an increase in free-stream turbulence delays the onset of stall and accelerates the reattachment of the boundary layer to the surface of the blades, affecting the critical azimuthal angles at which the turbine rotor interacts with the free-stream. The obtained wake flow fields at the optimal tip-speed ratio indicate that elevated levels of free-stream turbulence increase the streamwise velocity deficit, resulting in a delayed wake recovery. Additionally, increasing free-stream turbulence was shown to decrease the transition distance from near- to far-wake, while also reducing the total streamwise momentum recovery, indicating a reduction in the out-of-plane momentum transport, associated with quicker dissipation of blade tip-vortices.

These results offer practical implications for the design and implementation of tidal turbine. The addition of non-periodic loading and a decrease in the unloading period on the turbine blades may require a more robust turbine and system integration design, depending on the free-stream turbulence characteristics of the tidal environment. Furthermore, the change in momentum transfer rate in the wake of the turbine will require additional consideration for optimal turbine array spacing.

2.2 Keywords

H-Darrieus turbine; Cross-flow turbine; Wake structure; Power extraction performance; Turbulence; Particle image velocimetry; Experimental

2.3 Introduction

Hydrokinetic turbines are energy conversion devices that have potential to expand sustainable power production. Compared to axial-flow turbines, cross-flow turbines are receiving interest due to their relatively simple design [18], the surfeit of operational locations [15], and ease of manufacturability [19]. Both computational and experimental studies drive advancements in this field. As the number of turbine installations in rivers, streams, and tidal sites increases, there is a growing need to shift research towards accurately representing the real-world operating conditions encountered at these installation sites. Interest in how varying inflow conditions affect the performance and the wake structure of cross-flow turbines dates back to 1984, with Vittecoq and Laneville [20]. However, difficulty in replicating representative turbulent environments within laboratory settings or validating numerical studies continues to hinder progress.

Numerous studies have focused on the impact of turbulent inflow on the performance of cross-flow turbines. Notably, Bachant and Wosnik [21] experimentally found that power extraction of the turbine, when exposed to grid-generated inflow turbulence, provides marginally higher performance at lower tip-speed ratios (TSRs) and marginally lower performance at higher TSRs. Similarly, Baloutaki et al. [22] experimentally investigated the impact of grid-generated

turbulence on a cross-flow turbine. It was observed that increasing free-stream turbulence resulted in a substantial increase in power extraction performance. Möllerström et al. [23] also experimentally investigated the influence of turbulence on the power extraction of a cross-flow turbine, finding that, although minor, higher power production is achieved with elevated free-stream turbulence levels.

Numerous other studies have investigated both the performance and the wake structure of cross-flow turbines under elevated levels of free-stream turbulence. Peng and Lam [24] conducted both numerical and experimental investigations into the effect of free-stream turbulence on cross-flow turbines. It was concluded that an increase in free-stream turbulence significantly increases the power extraction performance of the turbine, as well as increases the wake recovery rate. Experimentally, Monlina et al. [25] found that elevated levels of free-stream turbulence provided a 20% increase in power extraction performance. Additionally, the wake was also observed to recover faster in a turbulent inflow. Carbo et al. [26] continued the experiments of Monlina et al. [25], expanding them to another testing location. It was found that inflow turbulence improved the power extraction performance by up to 20%, with this increase being more prevalent at lower tip speed ratios and lower Reynolds numbers. Sentchev et al. [27] carried out testing in the Scheldt estuary, concluding that power fluctuations increase with an increase in free-stream turbulence level. However, no notable change in turbine performance was observed. It was nonetheless found that the integral length scale of the turbulent inflow has a linear correlation with the magnitude of power fluctuations. In contrast, the numerical work of Dhalwala et al. [28] observed that turbine performance decreases under a turbulent inflow, with a minimal change in performance between an inflow of 5% and 10% turbulent intensity. An increase in power coefficient fluctuations was also noted. The wake of the turbine was reported to recover quickly in response to an increase in inflow turbulence. Hohman et al. [29] experimentally studied the effect of inflow conditions on the wake. While inflow conditions did not affect the overall wake structure, incoming turbulence was observed to decrease the strength of dynamic stall, resulting in a reduction in near-wake turbulence.

2.4 Turbine Dynamics

The complex, non-linear dynamics of cross-flow turbines are dependent on the continuously changing angle-of-attack and chord-based Reynolds number, defined as $Re_C = \rho U_{eff} C/\mu$, where ρ is the fluid density, U_{eff} is the effective flow velocity, C is the blade chord length, and μ is the fluid dynamic viscosity. Both the angle-of-attack and chord-based Reynolds number, Re_C, vary in a non-linear manner with the azimuthal angle and the angular velocity of the rotor. The angular velocity of the rotor is quantified by its TSR, a nondimensional ratio of the blade speed and the inflow velocity:

$$\mathrm{TSR} = \frac{\omega r}{U_\infty} \ , \tag{2.1}$$

where ω is the angular velocity of the rotor, r is the radius of the rotor, and U_∞ is the free-stream inflow velocity. From the blade kinematics for the rotor, depicted in Figure 2.1a, the effective angle-of-attack, $\alpha_{eff}(\theta)$, can be derived:

$$\alpha_{eff}(\theta) = tan^{-1}\left(\frac{sin\,\theta}{\mathrm{TSR} + cos\,\theta}\right), \tag{2.2}$$

where θ is the azimuthal angle of the rotor, defining the angle between the +Y-axis and the quarter chord of the blade under consideration. Another important metric is the effective flow velocity experienced by the blade:

$$U_{eff}(\theta) = U_\infty \sqrt{1 + 2\,\mathrm{TSR}\,cos\,\theta + \mathrm{TSR}^2}\ . \tag{2.3}$$

Using Eqn. (2.1), (2.2), and (2.3) presents two important plots that aid in understanding the complex dynamics of this system: the effective angle of attack and Re_C as functions of the rotor azimuth angle. Figure 2.1b shows the large variation in the angle-of-attack of the blade, greatly exceeding the static stall angle for the foil at lower TSRs. Figure 2.1c shows the variation of Re_C of the turbine blade over a rotation period. The variations of the angle-of-attack and Re_C illustrate the importance of TSR when investigating the impact of a turbulent inflow on the performance and wake characteristics of a cross-flow turbine.

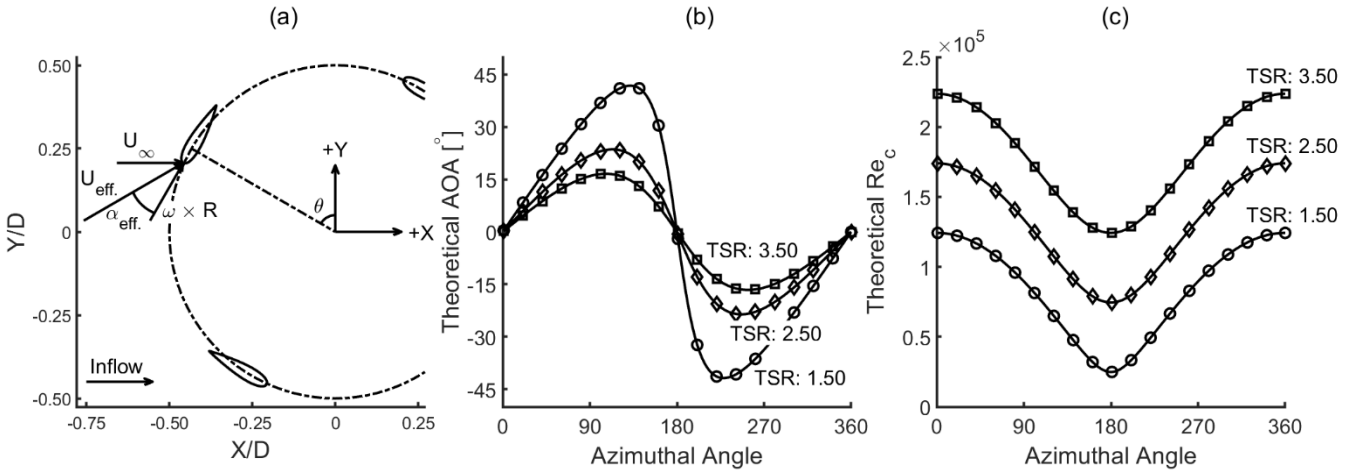

Figure 2.1: a) Blade kinematics, b) Theoretical angle-of-attack for varying tip-speed ratios, and c) Chord-based Reynolds number for varying tip-speed ratios.

Despite numerous investigations studying the effects of inflow turbulence on cross-flow turbines, a lack of consensus within the published results points to the necessity of a deeper insight into the response of a cross-flow turbine under varying inflow conditions. The objective of this study is to gain insight into the discrepancy observed in the literature, to identify the reasons for changes in power extraction performance and the mechanism responsible for momentum transfer in the wake of the turbine. This improved understanding is expected to inform design specifications, array placements, and integration considerations for the installation and operation of tidal turbines under realistic operating conditions.

2.5 Experimental System and Technique

2.5.1 Flow Facility

The experiments were conducted in a water channel at the University of Victoria's Fluid Mechanics Laboratory, depicted in Figure 2.2, which had a test section of 45 cm x 45 cm in cross-section and 2.5 m in length. A lid was installed on the water tunnel to allow for trivial pressurization, which effectively eliminated free surface effects. The water tunnel was controlled

by a variable-frequency drive operating a 25 hp motor-pump, which maintained the targeted inlet velocity of 1.6 m/s used in these experiments.

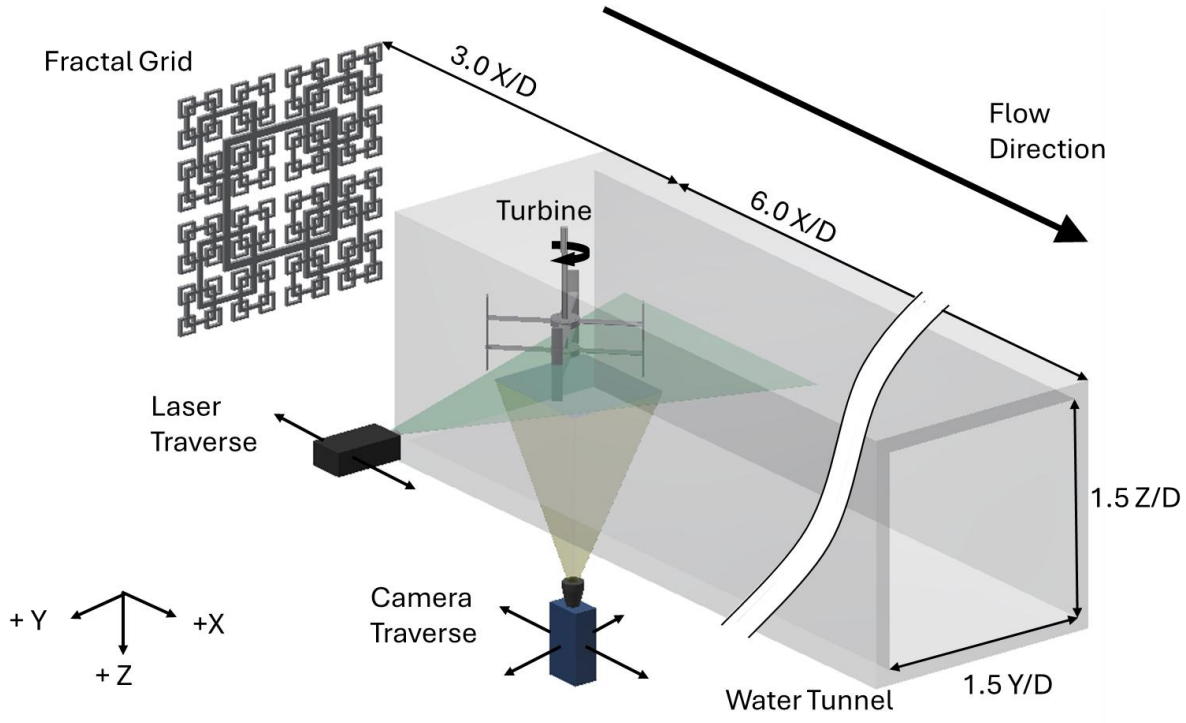

Figure 2.2:Experimental Setup overview. The Z-origin is located at the midspan of the turbine, where the X- and Y-origin are the centered on the turbine shaft. The dimensions shown are all nondimensionalized by the turbine diameter, D = 300 mm.

Upstream of the observation area, turbulence grids were installed to provide turbulent inflow into the test section. Square space-filling fractal grids were chosen for their high effectiveness in generating turbulence with a low blockage ratio [30]. Two different grids were used in conjunction with a baseline case (no turbulence grid) to provide three distinct inflow conditions. Figure 2.3 shows the space-filling fractal used for the intermediate turbulence case. The fractal grid used in the high turbulent case was also a 4-iteration grid, with both fractal grids designed to fit inside the water channel. The grids were characterized by a thickness ratio, defined as the ratio of the longest bar thickness to the smallest bar thickness, of 3.25 for the intermediate turbulent case and a thickness ratio of 13.0 for the high turbulent case. Both grid designs shared

a length ratio, the reduction multiple in length from between iteration, of 1/2, and a designed blockage ratio of 25%.

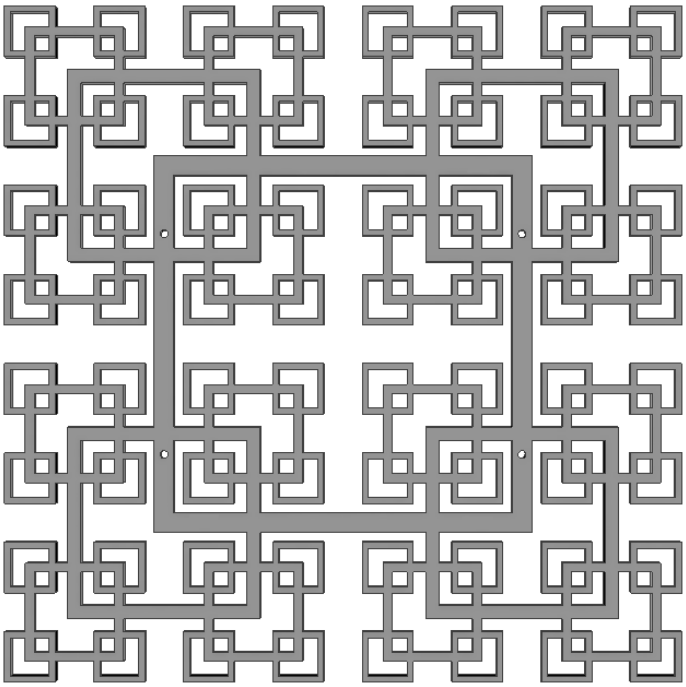

Figure 2.3: Space-filling fractal grid used in the intermediate turbulence case.

The actuation of the model H-Darrieus style cross-flow turbine used in the experiment is shown in Figure 2.4. The turbine model, installed 45 cm downstream of the test section inlet, had four blades with NACA 0021 profiles and chord lengths of 21 mm, a rotor height of 150 mm, and a rotor diameter of 300 mm, which produced a blockage ratio 22% in the tunnel cross-section. This turbine was fastened to a 16 mm diameter shaft that was fed through a hole in the roof of the water channel before fastening to a NEMA 23 servo motor and a 4 Nm NOVATECH reactionary torque transducer. The shaft of the turbine was outfitted with a 12-bit optical rotary encoder, which provided measurements of the absolute position of the turbine throughout its rotation. The acquisition of the signals from the servo motor, the encoder, and the torque transducer was performed using a National Instruments USB-6212 multifunction I/O device. The turbine actuation setup was tested to ensure consistent rotational behavior between the three turbulent conditions. It was determined that the turbine's angular velocity, actively controlled by the closed

loop servo motor, was able to hold the TSR to the specified value with a standard deviation of ±0.003.

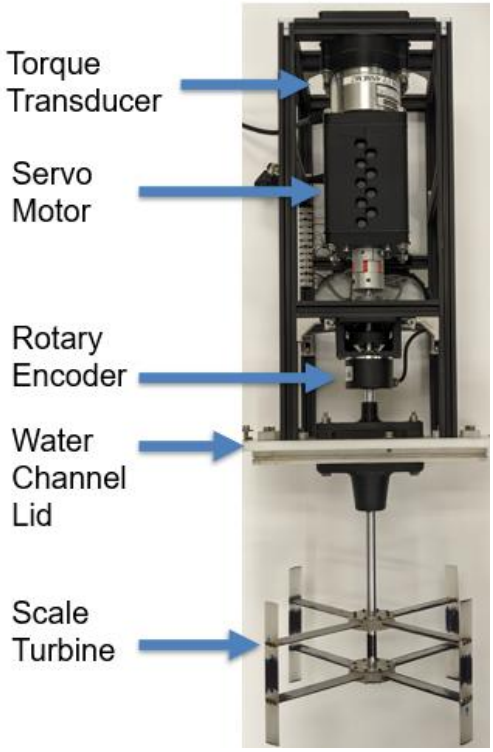

Figure 2.4: Turbine actuation apparatus.

2.5.2 Quantitative Flow Imaging

Planar Particle Image Velocimetry (PIV) was employed at the mid-height of the test section to obtain global, quantitative visualization of the wake of the turbine. The PIV system consisted of a Quantel Evergreen Nd: YAG 532 nm dual-pulsed laser for particle illumination, a LaVision SX 6M camera for capturing the images of the illuminated particles, and DaVis 10.1.2 software for data acquisition. The camera was fitted with a 28 mm, F2.8 lens to provide a field of view of 225 mm x 180 mm, corresponding to 2752 pixels x 2200 pixels.

The turbine was operated at TSR = 2.65, at which the turbine achieved the maximum power coefficient at the baseline turbulence case. At this TSR, 2000 randomly sampled PIV image sets were obtained alongside the encoder position, allowing for the ensembled- and phase-averaged velocity fields to be calculated. The sampled PIV Images were obtained by randomly selecting 2000 PIV trigger frequencies between 0.35-12.0 Hz, resulting in an average position sampling duration time of 10 minutes. The PIV camera was moved to 24 sequential positions, 2 cross-stream and 12 streamwise to yield a mosaic representation of the time- and phase-averaged wake structure, as shown in Figure 2.5.

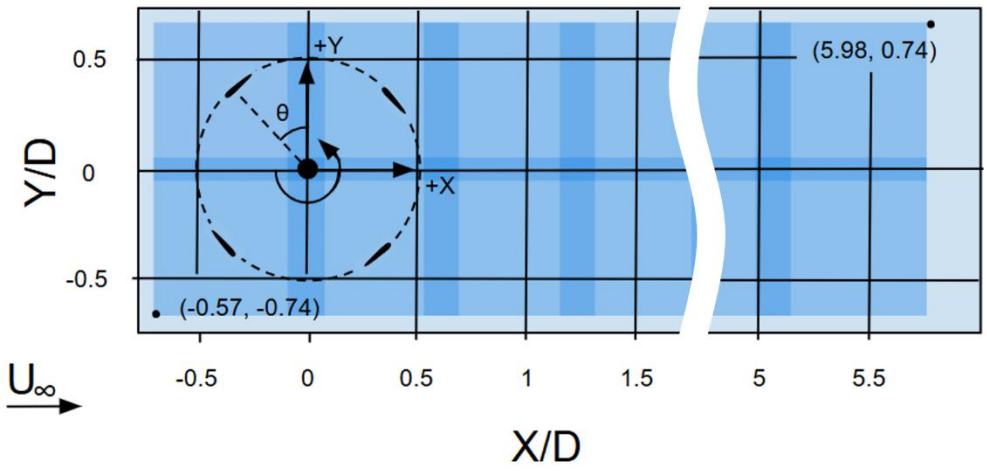

Figure 2.5: Mosaic representation of sequential PIV camera positions.

A multi-pass cross-correlation was conducted on the PIV images with an initial integration window size of 32 pixels x 32 pixels with no overlap that was subsequently reduced to a final interrogation window of 8 pixels x 8 pixels with a 50% overlap in both X- and Y-directions. The resultant velocity field had a vector pitch of 0.33 mm / vector with each vector having a spatial resolution of 0.66 mm / vector.

2.5.3 Inflow Characteristics

The power performance and wake structure of the turbine were studied for three distinct turbulent inflow conditions with the inflow turbulence intensities of: 1.4%, 4.7%, and 10.6%, summarized in Table 2.1. The turbulent properties of the inflow conditions are defined as follows.

The turbulence intensity, which is a measure of velocity fluctuations relative to the mean values, is defined according to Eqn. (2.4),

$$TI = \frac{\sigma}{U_\infty} \ , \tag{2.4}$$

where σ is the standard deviation of the mean velocity, computed from the standard deviations of the mean velocity components in the streamwise and cross-stream directions (σ_x and σ_y, respectively): $\sigma = \sqrt{\sigma_X^2 + \sigma_Y^2}$.

The turbulent kinetic energy is defined as:

$$TKE = \frac{1}{2}\sigma^2 \ . \tag{2.5}$$

The dissipation rate of turbulent kinetic energy, ϵ, was calculated using the Modified Spectra Curve Fit Method introduced by Xu and Chen [31]. Once the dissipation rate was acquired, the calculation of the three characteristic length scales was performed. The integral length scale, which is representative of the most energetic eddies in the turbulent flow, is defined by:

$$L = \frac{\sigma^3}{\epsilon} \ . \tag{2.6}$$

The Kolmogorov dissipation scale, which is a measure of the smallest coherent turbulent scale in flow, is defined by:

$$\eta = \left(\frac{\nu^3}{\epsilon}\right)^{\frac{1}{4}} \ , \tag{2.7}$$

where $\nu = 1.004 \times 10^{-6}\ \mathrm{m^2/s}$ is the kinematic viscosity of the working fluid. The Taylor microscale, an intermediate length scale responsible for the dissipation of turbulent energy, where the viscosity of the fluid significantly impacts the dynamics of the turbulent eddies in the flow, is defined as:

$$\lambda = \sqrt{\frac{15\nu}{\epsilon}}\sigma\ . \tag{2.8}$$

The Taylor-scale Reynolds number is defined as:

$$Re_\lambda = \frac{\lambda\sigma}{\nu}. \tag{2.9}$$

Table 2.1: Characteristics of the three inflow conditions: baseline, Intermediate, and high turbulence intensities.

Turbulent Case	U_∞ $[m/s]$	TI $[\%]$	TKE $[m^2/s^2]$	ϵ $[m^2/s^3]$	L $[mm]$	η $[mm]$	λ $[mm]$	Re_λ $[-]$
Baseline	1.60	1.4	0.0011	0.0572	0.7	0.065	0.549	18.3
Intermediate	1.60	4.7	0.0082	0.1280	6.0	0.053	0.967	86.4
High	1.60	10.6	0.0249	0.2064	15.3	0.049	1.206	190.4

2.5.4 Performance Characteristics of the Turbine

The performance of the turbine was monitored across the range of TSRs $1.0 < \mathrm{TSR} < 3.4$ in increments of $\Delta\mathrm{TSR} = 0.1$ for all three inflow conditions: baseline, intermediate, and high turbulence intensities. The channel velocity was kept constant at $U_\infty = 1.60$ m/s for all three inflow conditions, while the turbine encoder and the torque transducer were sampled at 250,000 Hz across 150 complete rotations of the turbine for each tip-speed ratio assessed. The power extraction performance of the turbine is represented by the power coefficient:

$$C_p = \frac{\omega\tau}{\frac{1}{2}\rho A_{proj.}U_\infty^3}\ , \tag{2.10}$$

where ω is the angular velocity of the turbine, τ is the average torque of the turbine over a period of rotation, ρ is the density of the fluid, and $A_{proj.}$ is the projected frontal area of the turbine, equal to the product of the diameter and the height of the rotor. The torque was initially measured for the shaft without the rotor. This value was subtracted from the torque obtained with the rotor attached.

2.6 Results

2.6.1 Power Extraction Performance

The power extraction performance of the turbine is illustrated by plotting the C_p against an incrementally increasing TSR, displayed in Figure 2.6 for each of the three tested inflow conditions. Each data point represents the cycle-averaged C_p of the turbine at the corresponding TSR.

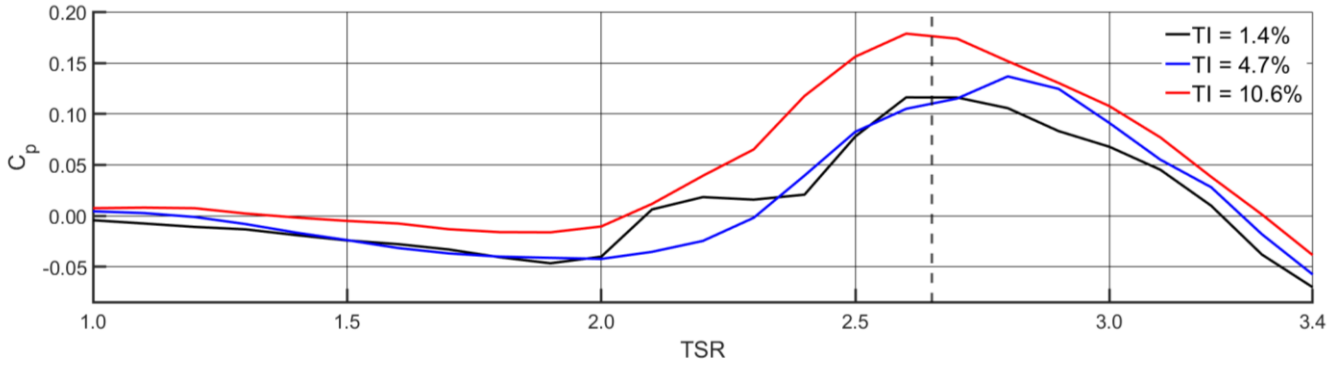

Figure 2.6: Power coefficient as a function of tip-speed ratio for three inflow conditions: baseline TI = 1.4% (black), intermediate TI = 4.7% (blue), and high TI = 10.6% (red). The maximum C_p achieved by the baseline case is marked by the dashed vertical line (TSR = 2.65).

The power extraction curves revealed a substantial variation in performance across the range of the considered TSRs. The baseline turbulence case produced a peak C_p = 0.12 at TSR = 2.65. In comparison, the intermediate turbulence case produced a maximum C_p = 0.14 at TSR = 2.80, corresponding to a 17% increase in peak performance. The high turbulence case produced a maximum C_p = 0.18 at TSR = 2.60, corresponding to a 54% increase in peak performance relative to the baseline case. At TSR = 2.65, defined by the TSR at which the baseline case achieved maximum power extraction, the intermediate turbulence case produced C_p = 0.11, resulting in a decrease in performance of 11% compared to the baseline case. In contrast, the high turbulence case produced C_p = 0.18 at TSR = 2.65, corresponding to the 54% increase in power coefficient compared to the baseline case.

To provide additional insight into the intracycle effect of the freestream turbulence, we considered the azimuthal positions at which the power coefficient reached its minimum and maximum values, denoted by $C_{p_{Min}}$ and $C_{p_{Max}}$, respectively. Figure 2.7 shows the variation of the azimuthal angles of the rotor, θ, corresponding to the occurrences of $C_{p_{Min}}$ and $C_{p_{Max}}$ as functions of the TSR.

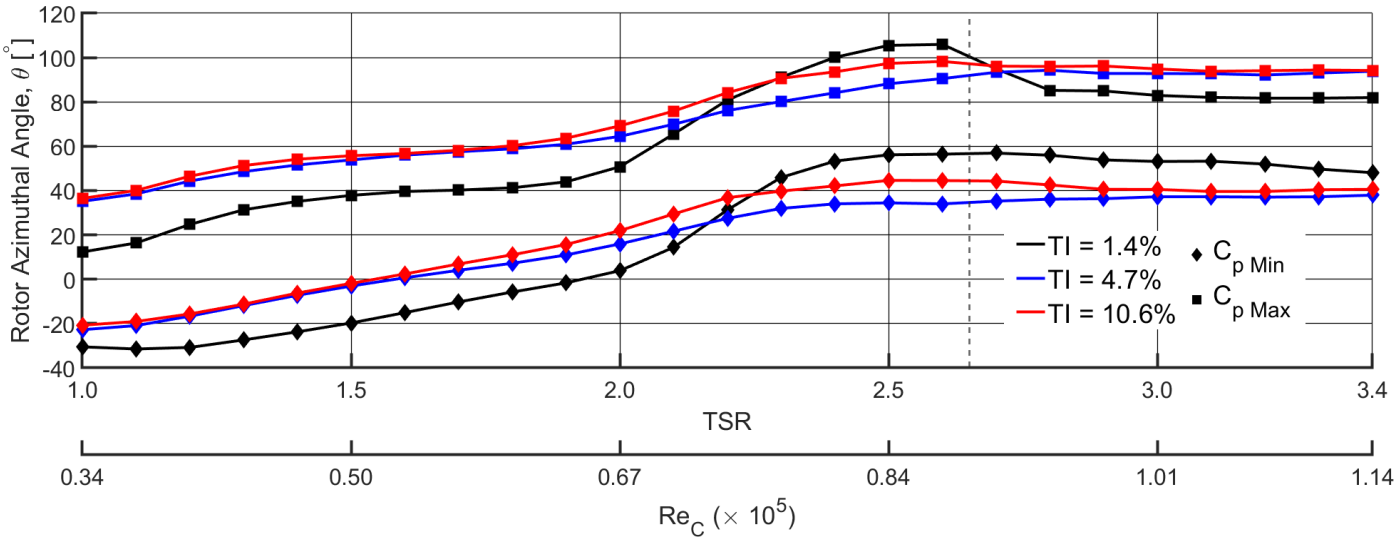

Figure 2.7: Azimuthal angles of the rotor corresponding to occurrences of $C_{p_{Min}}$ and $C_{p_{Max}}$ as functions of the TSR for the three inflow conditions: baseline TI = 1.4% (black), intermediate TI = 4.7% (blue), and high TI = 10.6% (red). The maximum C_p achieved by the baseline case is marked by the dashed vertical line (TSR = 2.65).

The azimuthal angle of $C_{p_{Min}}$ initially increased with TSR for all three inflow conditions, plateauing at a TSR of approximately 2.30 to 2.40. The azimuthal angle of $C_{p_{Max}}$ followed a similar trend, with the plateau establishing at TSR $\approx$ 2.60. For TSR $\geq$ 2.60, $C_{p_{Max}}$ gradually decreased. For 2.60 < TSR < 3.4, the mean azimuthal angle of $C_{p_{Max}}$ is $83°$ in the baseline turbulence case, $89°$ for the intermediate turbulence case, and $92°$ for the high turbulence case. For 2.40 < TSR < 3.4, the mean azimuthal angle of $C_{p_{Min}}$ is $54°$ for the baseline turbulence case, $38°$ for the intermediate turbulence case, and $42°$ for the high turbulence case. These trends indicate that increasing inflow turbulence broadens the azimuthal range between the observed $C_{p_{Min}}$ and $C_{p_{Max}}$, suggesting a larger window of power extraction.

The power extraction curves and the azimuthal angles of $C_{p_{Min}}$ and $C_{p_{Max}}$ are ideal for characterising rotor performance at various TSRs. For a more comprehensive picture of the effect of turbulence, the instantaneous C_p as a function of azimuthal angle is considered TSR = 2.65, displayed in Figure 2.8. The black line in each plot represents the instantaneous C_p at the corresponding azimuthal angle, averaged over 150 rotations. The coloured bands: grey in Figure 2.8a, blue in Figure 2.8b, and red in Figure 2.8c, represent the 95% confidence interval computed from the variability of C_p across 150 rotations.

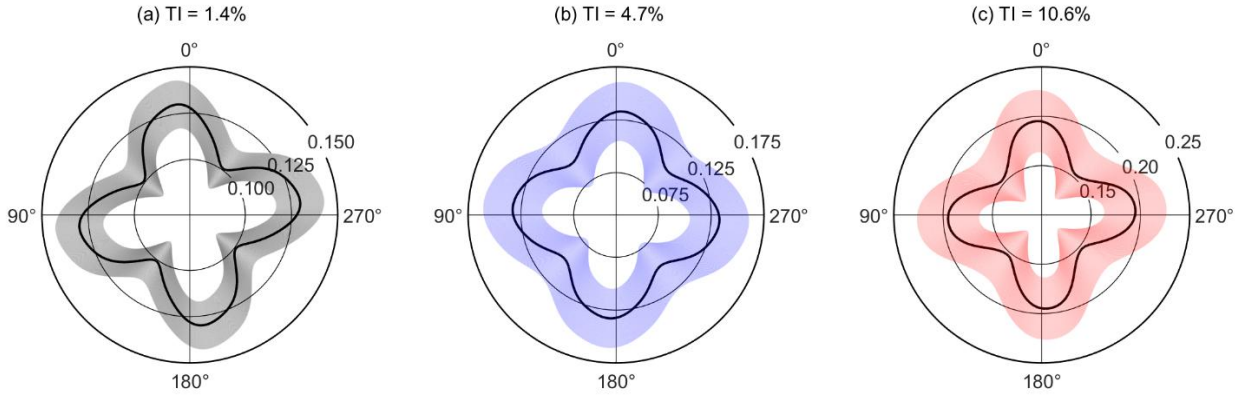

Figure 2.8: Instantaneous C_p as a function of azimuthal angle, at TSR = 2.65 for the three inflow conditions : a) baseline TI = 1.4% (black), b) intermediate TI = 4.7% (blue), and c) high TI = 10.6% (red). The solid black line represents the average C_p at the indicated azimuthal angle, and the coloured bands represent the 95% confidence interval of C_p.

While Figure 2.7 illustrated that the intermediate turbulence case has a larger azimuthal range between $C_{p_{Min}}$ and $C_{p_{Max}}$ compared to the baseline turbulence case, it is observed in Figure 2.6 that the baseline turbulence case maintained a higher mean C_p compared to the intermediate turbulence case. Figure 2.8 shows the 95% confidence interval for the intermediate case is 25% greater relative to the baseline case, while the high turbulence case showed a 68% increase in confidence interval range compared to the baseline case, with a larger amplitude of C_p variation over the cycle of rotation. The increased azimuthal C_p variation with elevated inflow turbulence is linked to increased cycle-to-cycle variability of the flow pattern, indicating a growth of quasi-periodicity in the power extraction behavior of the turbine.

2.6.2 Wake Structure

The variation in instantaneous C_p under elevated levels of free-stream turbulence at the TSR = 2.65 resulted in the three distinctive azimuthal power extraction profiles, shown in Figure 2.8. To better understand how these profiles influence the wake structure of the turbine, the wake was investigated at downstream from the turbine, where the velocity components in the streamwise and cross-stream directions were nondimensionalized by the free-stream velocity, resulting in the velocity deficit presented in Figure 2.9.

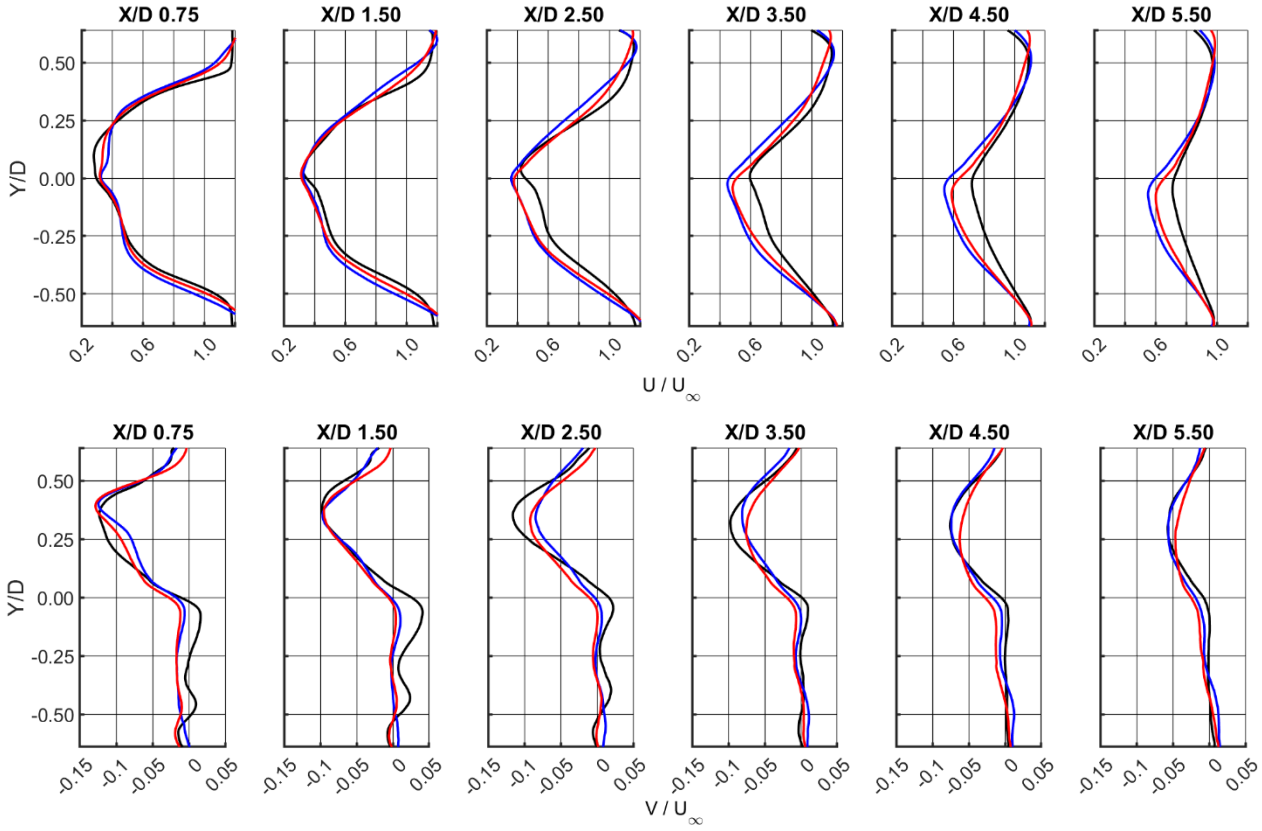

Figure 2.9: Nondimensionalized velocity contours in the wake of the turbine for the three operating inflow conditions: baseline TI = 1.4% (black), intermediate TI = 4.7% (blue), and high TI = 10.6% (red). The Top row: the streamwise (X-directional) velocity component. Bottom row: the cross-stream (Y-directional) velocity component. The rotor axis is located at X/D = 0.

The streamwise velocity contours in the wake of the turbine, presented in Figure 2.9, revealed a slower wake recovery rate in the elevated turbulent cases when compared to the baseline turbulent case. At X/D = 5.50, at the centre of the wake, Y/D = 0, the streamwise velocity component recovered to 87% of the freestream velocity value in the baseline case (TI = 1.4%), but only to 54% and 60% in the intermediate (TI = 4.7%) and high (TI = 10.6%) turbulence cases, respectively. Additionally, the elevated turbulent inflow cases displayed a wider cross-stream wake, consistent with an increase in wake entrainment. The cross-stream velocity deficit showed a contrasting trend, with the intermediate and high turbulence cases displaying a smaller velocity deficit compared to the baseline turbulence case. The baseline turbulent case also exhibited a positive streamwise velocity on the downward side of the turbine, Y/D < 0, which was absent in the two elevated turbulence cases.

The ensemble-averaged velocity contours of the wake in Figure 2.9 did not capture the persistence of velocity fluctuations within the wake. The dissipation of these fluctuations marks the near- to far-wake transition of the turbine's wake. To quantify this transition, proper orthogonal decomposition (POD) was performed on the fluctuating component of the velocity magnitude, organized from 0° to 360°. A non-uniform discrete Fourier transform was performed on the first 6 POD temporal bases to extract the wake frequency. These frequencies were then normalized such that the sum of wake oscillation amplitudes at the downstream distance 0.5 X/D is equal to unity. Decomposing the wake with this method enabled a direct comparison of the decay of the oscillations in the wake of the turbine, as shown in Figure 2.10. On the Y-axis in Figure 2.10, a normalized wake frequency of 4 represents the blade passing frequency of the rotor. In the baseline case, this mode dissipated to 95% of its original energy at X/D = 1.65. In the intermediate turbulence intensity case, this threshold was reached 21% faster, at X/D = 1.30, and the high turbulence case exhibited transition to far-wake 28% faster than the baseline case at X/D = 1.18.

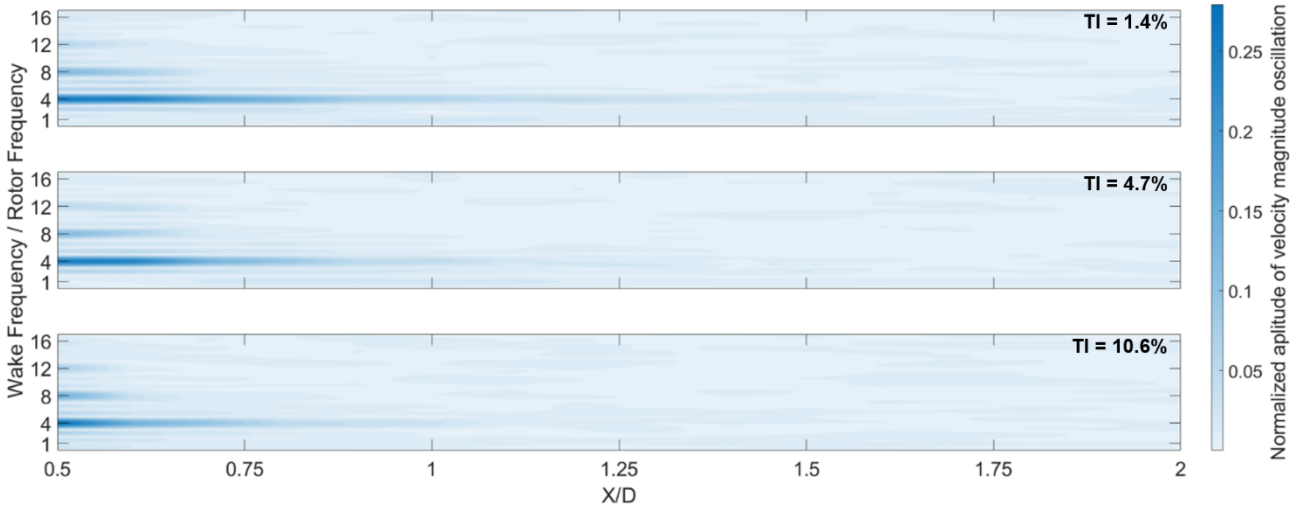

Figure 2.10: Normalized streamwise frequency of velocity magnitude oscillations, averaged in the cross-stream direction as a function of the downstream distance for the three turbulent inflow conditions: baseline TI = 1.4% (top), intermediate TI = 4.7% (middle), and high TI = 10.6% (bottom). The rotor axis is located at X/D = 0.

While Figure 2.9 and Figure 2.10 illustrate the change in the mean velocity and the mean frequency at various downstream locations, additional insight into the wake recovery can be obtained by analysing the wake momentum budget. The budget is obtained by rearranging the Reynolds-averaged Navier-Stokes (RANS) equations as follows:

$$\overbrace{\frac{\partial \bar{U}}{\partial X}}^{1} = \frac{1}{\bar{U}}\left[\underbrace{\overbrace{-\bar{V}\frac{\partial \bar{U}}{\partial Y}}^{2}\overbrace{-\bar{W}\frac{\partial \bar{U}}{\partial Z}}^{3}}_{Advection} \underbrace{\overbrace{-\frac{1}{\rho}\frac{\partial P}{\partial X}}^{4}}_{Pressure\ gradient} \underbrace{\overbrace{-\frac{\partial}{\partial X}\overline{U'U'}}^{5}\overbrace{-\frac{\partial}{\partial Y}\overline{U'U'}}^{6}\overbrace{-\frac{\partial}{\partial Z}\overline{U'U'}}^{7}}_{Reynolds\ stresses} + \underbrace{\nu\left(\overbrace{\frac{\partial^2 \bar{U}}{\partial X^2}}^{8} + \overbrace{\frac{\partial^2 \bar{U}}{\partial Y^2}}^{9} + \overbrace{\frac{\partial^2 \bar{U}}{\partial Z^2}}^{10}\right)}_{Viscous\ stresses}\right]. \qquad (2.11)$$

Each of the numbered segments comprising Eqn. (2.11) is nondimensionalized using the diameter of the turbine and the free-stream velocity. This procedure quantifies the individual contributions of advection, pressure gradient, Reynolds stresses, and viscous stresses to the wake recovery. Figure 2.11 shows terms 1, 2, 8, and 9 from Eqn. (2.11) as functions of the downstream distance, while terms 5 and 6 are omitted as they had a negligible impact.

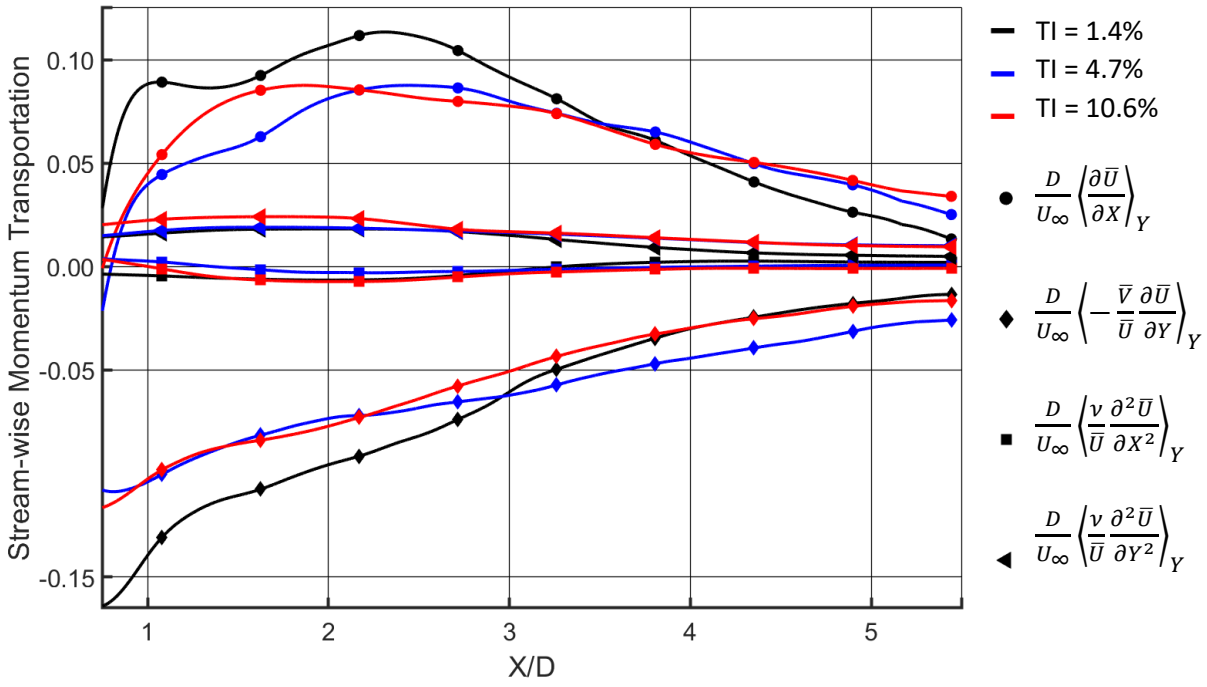

Figure 2.11: Nondimensionalized streamwise (X-directional) momentum transport components at the midspan of the turbine, averaged in the cross-stream direction as functions of the downstream distance for the three turbulent inflow conditions: baseline TI = 1.4% (black), intermediate TI = 4.7% (blue), and high TI = 10.6% (red). The rotor axis is located at X/D = 0.

The total streamwise velocity recovery rate, $\frac{D}{U_\infty}\left\langle\frac{\partial \bar{U}}{\partial X}\right\rangle_y$, indicated by circular symbols in Figure 2.11, illustrated that the baseline turbulence case had a peak recovery rate that was higher than that of the intermediate and high turbulence cases by 60% and 63%, respectively. The peak in recovery rate occurred at TSR = 2.4 for the baseline turbulence case, TSR = 2.6 for the intermediate turbulence case, and TSR = 1.9 for the high turbulence case. Furthermore, by

evaluating the computable transportation terms on the right-hand side of Eqn. (2.11), terms 2, 5, 6, 8, and 9, and subtracting them from the total momentum transfer on the left-hand side of Eqn. (2.11), term 1, the residual of transportation terms are left on the right-hand side of Eqn. (2.11), comprised of terms 3, 4, 7, and 10. This remainder, which cannot be computed using the current data set, is attributed to the combination of the axial (Z-directional) advection, the streamwise pressure gradient transportation, the axial Reynolds stresses, and the axial viscous stresses. The combination of terms that collectively contribute to the residual in recovery rate between the three turbulence cases is plotted in Figure 2.12.

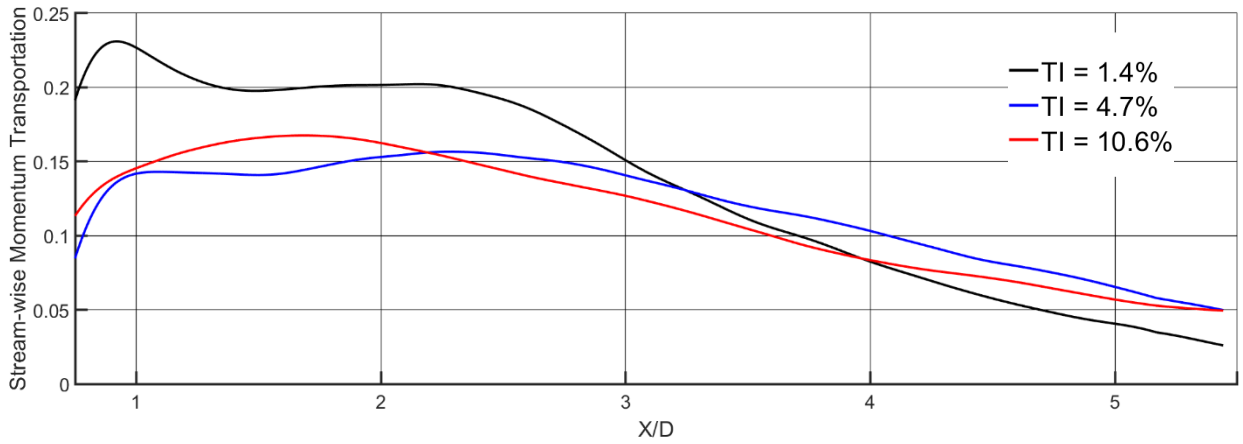

Figure 2.12: Nondimensionalized remainder of the streamwise (X-directional) momentum transport (terms 3,4,7, and 10 of Eqn. (2.11) at the midspan of the turbine, averaged cross-stream (Y-directional) as a function of the downstream position for the three turbulent inflow conditions: baseline TI = 1.4% (black), intermediate TI = 4.7% (blue), and high TI = 10.6% (red). The rotor axis is located at X/D = 0.

The residual transportation term in Figure 2.12 illustrate the combined effect of the out-of-plane momentum transport terms and the streamwise pressure gradient. Upstream of X/D = 3, the baseline turbulence case exhibited a greater contribution to the wake recovery from these residual terms when compared to the two elevated turbulence cases. The interval $3 < X/D < 4$ is a transition region, where the contribution of the residual term in the baseline case decayed faster than that in the two elevated turbulence cases. Downstream of X/D = 4, the intermediate and the high turbulence cases experienced a greater contribution to the wake recovery rate from

the residual terms than the baseline turbulence case. A similar trend was observed in the total streamwise wake recovery rate, $\frac{D}{U_\infty}\left\langle\frac{\partial \bar{U}}{\partial X}\right\rangle_y$ in Figure 2.11.

2.7 Discussion

2.7.1 Power Performance

The observed increase in maximum power extraction performance of the turbine with increasing free-stream turbulence, shown in Figure 2.6, is consistent with several studies on the topic: [22], [24], [25], [26]. This behaviour is often attributed to the turbine operating at a chord-based Reynolds number below $(Re_c <)\ 2 \times 10^5$. This Reynolds number threshold, identified experimentally by Bachant and Wosnik [32], aligns with blade boundary layer theory. Specifically, it marks the consistent transition from a laminar to a turbulent flow regime within the blade boundary layer [33], indicating the reliable reattachment of the mid-chord laminar separation [34]. Before this Reynold independence threshold, there is one further critical chord-based Reynolds number, taking place at 0.7×10^5 [33]. This is the Reynolds number at which the performance of a hydrofoil in a laminar flow first experiences an abrupt increase in lift-to-drag ratio due to the possibility for reattachment of the laminar separation bubble [34].

The turbine in this study achieved a critical chord-based Reynolds number of 0.7×10^5 at a TSR of approximately 2.00. A dramatic improvement in blade performance was observed in Figure 2.6 for the baseline turbulence case. This critical Reynolds number was also observed for the baseline case in Figure 2.7, with a sharp increase in the turbine's azimuthal interaction angles, $C_{p_{Min}}$ and $C_{p_{Max}}$. Most notably in this operating range, the two elevated turbulence cases, in contrast to the baseline case, did not exhibit this exaggerated phase increase. This observation suggests that the effect of elevated free-stream turbulence may mimic the effect of increased Reynolds number, as noted by Yap et al. [35].

Assuming that the effect of elevating free-stream turbulence is analogous to increasing the Reynolds number, it was expected that the intermediate turbulence case would exhibit in-between power performance relative to the baseline and the high turbulence cases. However,

this trend was not observed in the lower range of the tested TSRs. One possible rationale is the presence of a longer laminar separation bubble in the intermediate turbulence case, compared to the high turbulence case. This hypothesis is supported by Damiola et al. [36], who observed that, at this Reynolds number, low turbulent inflow regimes are associated with abrupt stall, while higher levels of free-stream turbulence led to a more gradual stall behaviour.

At and above TSR = 2.65, approaching a Reynolds independence regime, Figure 2.7 showed that the azimuthal angles of $C_{p_{Min}}$ and $C_{p_{Max}}$ plateaued for all three inflow conditions considered. This figure also demonstrates that elevated levels of free-stream turbulence extend the azimuthal region between $C_{p_{Min}}$ and $C_{p_{Max}}$, allowing for a longer azimuthal power extraction window. This is evident from the higher $C_{p_{Max}}$ in elevated turbulent cases relative to the baseline case, indicating delayed stall and faster boundary layer recovery, supported by a lower $C_{p_{Min}}$ in the elevated cases. Similar observations were noted by Huang et al. [37] and Damiola et al. [36], and can be directly observed from Figure 2.8, where the broadening of the azimuthal range between $C_{p_{Min}}$ and $C_{p_{Max}}$ is evident with increasing free-stream turbulence.

The 95% confidence interval of the mean power extraction at TSR = 2.65 was shown to increase with an increasing turbulence level, as shown in Figure 2.8. This trend is consistent with the findings from Bachant and Wosnik [21], Sentchev et al. [27], and Dhalwala et al. [28]. Additionally, it was observed that increasing free-stream turbulence increased the quasi-periodicity in the turbine's operation, resulting in greater azimuthal variance in the power extraction. As a result, the mean power coefficient profile of the elevated turbulence cases in Figure 2.8 appear more sinusoidal. However, this is not due to the turbine becoming more periodic; rather, a significant increase in cycle-to-cycle variability causes the averaging process to flatten irregular fluctuations in a way that represents a smoother and more periodic trend.

2.7.2 Wake Structure

The larger azimuthal variance in the power extraction at elevated free-stream turbulence levels was attributed to the increased quasi-periodicity in the shedding of leading- and trailing-edge

vortices. This behaviour was expected to broaden the velocity deficit behind the turbine and suppress the dominant frequencies in the near-wake. Streamwise velocity contours in Figure 2.9 confirm this with a more prominent deficit directly behind the turbine for the elevated free-stream turbulence cases. Additionally, dominant oscillatory structures in the turbine's wake, as shown in Figure 2.10, illustrated reduced downstream penetration of coherent structures with elevated free-stream turbulence, consistent with work from Dhalwala et al. [28].

Regarding the wake recovery, it was observed from Figure 2.9 that elevated free-stream turbulence levels resulted in a slower recovery. A wake momentum budget, similar to Bachant and Wosnik [32] and Boudreau and Dumas [38], was used to quantify the momentum transfer and the wake recovery rate. Although the analysis was restricted to a two-dimensional observation plane, the results suggest that the primary difference in wake recovery between the elevated and baseline turbulence cases is due to out-of-plane (axial) recovery mechanisms. Previous studies have identified tip-vortices as the primary wake recovery mechanism in cross-flow turbines [38], [39]. These tip-vortices have also been suggested as the cause of the asymmetry in the wake of the turbine [40], [29]. At elevated levels of turbulence, blade tip-vortices have been shown to dissipate more quickly [41], [42], suggesting that the dissipation rate difference between a moderate or intermediate and high turbulent inflow diminishes. This explanation is supported by the observation of a more symmetric wake observed in this study under elevated turbulence levels. The significant change in tip-vortex dissipation from a baseline to an intermediate turbulent regime, followed by a slight change in dissipation from the intermediate to high turbulence regime, offers a plausible explanation for the wake recovery trend observed. Specifically, the higher turbulence case recovers more quickly than the intermediate case, while both elevated cases appear to recover more slowly than the baseline case, supporting the hypothesis that the faster wake recovery in the higher turbulence case is due to higher entrainment and increased turbulent kinetic energy.

2.8 Conclusions

This study focused on the power extraction performance and wake structure of an H-Darrieus cross-flow turbine subjected to three distinct turbulent inflow conditions. These conditions were achieved experimentally through the installation of fractal grids upstream of the model turbine inside a water flume. Performance data across a broad range of TSRs was collected with a torque transducer, and the characterization of both the turbulent inflow characteristics and wake of the turbine was obtained using PIV at the mid-span of the turbine at TSR = 2.65.

The performance data emphasized the complex and non-linear effect of free-stream turbulence on the turbine's operation, particularly at low Reynolds numbers near the Reynolds number independence threshold. Elevated free-stream turbulence levels enhance power extraction by promoting accelerated boundary layer reattachment and delaying stall by suppression of the laminar separation bubble on the blades. However, performance trends with varying TSR appeared to follow no distinct trend, suggesting that small changes in inflow turbulence can amplify the effect on the blade boundary layer development and stall characteristics. At TSR = 2.65, elevated levels of turbulence resulted in a larger azimuthal extraction window and greater cycle-to-cycle variability, demonstrating an increase in quasi-periodicity. Although a larger extraction window has the potential to increase the power extraction performance, the linked increase in quasi-periodicity introduces challenges for electrical system integration and elevated turbine fatigue, emphasizing the importance of understanding the unsteady loading effects on the turbine.

In the wake of the turbine, the observed increase in quasi-periodicity, as presented in the performance data, resulted in a shorter near- to far-wake transition distance, attributed to the dampened downstream propagation of coherent flow structures. However, a lengthened far-wake recovery distance was revealed in elevated free-stream turbulence cases. A wake momentum budget revealed that the decrease in recovery rate is attributed to a decrease in out-of-plane (axial) momentum transport. The observed wake dynamics suggest a non-linear relationship between wake dissipation and free-stream turbulence characteristics, further

highlighting the need for additional consideration when determining inter-turbine spacing for array configurations.

The performance and wake findings jointly demonstrate that free-stream turbulence levels influence and alter the performance curves and wake characteristics in a highly non-linear and complex way. As a result, blade boundary layer and performance should be carefully considered in the design, development, and installation of cross-flow turbines, particularly in array configurations where wake-turbine interactions are unavoidable.

Chapter 3: Conclusions

The effects of free-stream turbulence on the power extraction performance and the wake structure of a cross-flow turbine are areas that require further development. The growth of this topic will enable more precise estimations of power conversion from tidal events, allowing engineers to account for additional fatigue loads, facilitate electrical integration with existing infrastructure, and inform decisions regarding intra-device spacing in tidal arrays. Strengthening any one of the aforementioned areas ensures steady progress in the development of renewable technology, a crucial step in achieving a diversified power grid and reducing reliance on fossil fuels. This Thesis sought to support existing literature and provide insight into the effects of turbulence with an experimental study.

3.1 Summary

Chapter 1: introduced cross-flow turbines, providing an overview of their advantages compared to other renewable technologies, as well as a comparison with the more commonly deployed hydrokinetic energy converter, the axial-flow turbine. Motivations for this research were presented, and the remainder of the thesis structure was outlined.

Chapter 2: of the thesis presented and discussed a manuscript draft relating to the impact of inflow turbulence on the power extraction performance and wake structure of a cross-flow turbine. A review of applicable literature on the topic was presented at the beginning of the manuscript. The experimental setup was introduced next, depicting the placement of the turbulence-generating grids, the turbine, and the PIV system. The turbulence characteristics for each of the turbulent intervals subjected to the turbine were then outlined. The presentation of the experimental results followed for both the power extraction performance and the wake structure of the turbine. Next, the discussion of results was given. It was concluded that the power extraction performance of the turbine under a turbulent inflow is sensitive to inflow conditions at an experimental diameter-based Reynolds number of 0.5×10^6. It was observed that an increase in turbulence intensity improved the power extraction performance of the turbine, which is thought to be the result of the laminar separation bubble hardening. The wake

structure of the turbine discussion, followed by the main findings, outlines the out-of-plane or axial-momentum in the wake being the most significant contributor to the wake's momentum recovery. Conclusions ended chapter two, summarizing that the effects of turbulence impact turbine array placement, power grid integration, design, and power estimations of the turbine, further promoting the need to advance this area of research.

3.2 Future Work

Improving estimates of the power extraction performance and wake structure of an H-Darrieus turbine subjected to free-stream turbulence remains an area with potential for growth. This study supports blade tip-vortices being the likely leading transport mechanism affecting the wake recovery of the turbine. The present study was limited to planar PIV, allowing for only direct measurements of the in-plane momentum transportation. The spatial and temporal resolutions were limited to 0.33 mm/vector and 12 Hz, respectively. Addressing each of these three main limitations of the study comprises a path forward in future work.

The two-dimensional observation limitations within this study arise from the acquisition of only the streamwise and cross-stream wake of the turbine, leaving the axial component untouched. Therefore, the first recommendation for future work is to address this limitation and extend the study to investigate the out-of-plan effects of turbulence. Furthermore, focusing on investigating the effects of freestream turbulence on tip-vortices at various inflow turbulence levels and TSRs would be beneficial in establishing a relationship regarding the coherence of wake dynamics.

The temporal resolution in this study was limited by the choice of camera, selected to balance temporal and spatial resolution. While the spatial resolution used in this thesis was sufficient to capture the near- and far-wake dynamics, focusing on the near-wake with a higher temporal resolution would allow for vortex tracking and monitoring of the inner rotor dynamics. The ability to track vortical structures is beneficial as the shed leading and trailing edge vortices are the significant sources of coherent structures in the wake of the turbine. Tracking of coherent structures also enables investigation into transients observed in the power extraction

performance data, as well as direct observations of blade vortex interactions that may occur, directly altering the wake dynamics.

The last limitation to discuss is the spatial resolution. Increased spatial resolution enables observations into the blade boundary layer at various azimuthal angles. This additional spatial resolution is beneficial as it provides direct visual access to the boundary layer response of the blade subjected to the turbulence intervals presented. A visible boundary layer enables the quantification of characteristics related to reattachment, laminar separation bubbles, and the roll-up of the leading-edge vortex. These boundary layer features can be used in conjunction with the apparent blade Reynolds number, supporting the analysis of the boundary layer and the Reynolds independence of the blades.

Bibliography

[1] Enerdata, "World Energy & Climate Statistics - Yearbook 2023," 2023. [Online]. Available: https://www.enerdata.net/publications/world-energy-statistics-supply-and-demand.html.

[2] Energy Institute, "Statistical Review of World Energy 2023," Energy Institute, London, 2023.

[3] United Nations, "Causes and Effects of Climate Change," 1 March 2022. [Online]. Available: https://www.un.org/en/climatechange/causes-and-effects-climate-change. [Accessed 14 June 2023].

[4] Goverment of Canada, "Causes of Climate Change," 19 March 2019. [Online]. Available: https://www.canada.ca/en/environment-climate-change/services/climate-change/causes.html. [Accessed 14 June 2023].

[5] G. N. Plass, "The Carbon Dioxide Theory of Climate Change," *Tellus,* vol. 8, no. 2, pp. 140-152, 1956.

[6] International Hydropower Association, "World Hydropower Outlook 2025," June 2025. [Online]. Available: https://www.hydropower.org/publications/2025-world-hydropower-outlook. [Accessed 13 August 2025].

[7] Global Wind Energy Council, "Global Offshore Wind Report 2024," April 2025. [Online]. Available: https://www.gwec.net/reports/globaloffshorewindreport/2024#Download. [Accessed 13 August 2025].

[8] International Renewable Energy Agency (IRENA), "Renewable Power Generation Costs in 2024," July 2025. [Online]. Available: https://www.irena.org/Publications/2025/Jun/Renewable-Power-Generation-Costs-in-2024. [Accessed 13 August 2025].

[9] R. F. Nicholls-Lee and S. R. Turnock, "Tidal energy extraction: renewable, sustainable and predictable," *Science Progress,* vol. 91, no. 1, pp. 81-111, 2008.

[10] N. D. Laws and B. P. Epps, "Hydrokinetic energy conversion: Technology, research, and outlook," *Renewable and Sustainable Energy Reviews,* vol. 57, no. 1, pp. 1245-1259, 2016.

[11] H. Québec, "A Renewable Energy Option," 2021. [Online]. Available: https://www.hydroquebec.com/data/developpement-durable/pdf/file-hydrokinetic-2021.pdf. [Accessed 9 February 2022].

[12] P. Fraenkel, "Practical tidal turbine design considerations: a review of technical alternatives and key design decisions leading to the development of the SeaGen 1.2MW tidal turbine," in *Ocean power: fluid machinery*, London, 2010.

[13] P. Bachant and M. Wosnik, "Performance measurements of cylindrical- and spherical-helical cross-flow marine hydrokinetic turbines, with estimates of exergy efficiency," *Renewable Energy,* vol. 74, no. 1, pp. 318-325, 2015.

[14] B. Kirke, "Towards more cost-effective river hydrokinetic turbines," *Energy for Sustainable Development,* vol. 78, no. 1, p. 101370, 2024.

[15] G. Li, G. Wu, L. Tan and H. Fan, "A Review: Design and Optimization Approaches of the Darrieus Water Turbine," *Sustainability,* vol. 15, no. 14, p. 11308, 2023.

[16] A. Zarketa-Astigarraga, M. Penalba, A. Martin-Mayor and M. Martinez-Agirre, "Impact of turbulence and blade surface degradation on theannual energy production of small-scale wind turbines," *Wind Energy,* vol. 26, no. 12, pp. 1213-1317, 2023.

[17] P. Druault, B. Gaurier and G. Germain, "Impact of varying turbulent flow conditions on the tidal turbine blade load fatigue," *Renewable Energy,* vol. 251, no. 1, p. 123370, 2025.

[18] M. M. Al-Rawajfeh and M. R. Gomaa, "Comparison between horizontal and vertical axis wind turbine," *Applied Power Engineering,* vol. 12, no. 1, pp. 13-23, 2023.

[19] P. M. Kumar, K. Sivalingam, S. Narasimalu, T.-C. Lim, S. Ramakrishna and H. Wei, "A Review on the Evolution of Darrieus Vertical Axis Wind Turbine: Small Wind Turbines," *Journal of Power and Energy Engineering,* vol. 07, no. 04, pp. 27-44, 2019.

[20] G. Brochier, P. Fraunie and C. Beguier, "Water Channel Experiments of Dynamic Stall on Darrieus Wind Turbine Blades," *Journal of Propulsion and Power,* vol. 2, no. 5, pp. 445-449, 1986.

[21] P. Bachant and M. Wosnik, "Experimental investigation of helical cross-flow axis hydrokinetic turbines, including effects of waves and turbulence," in *ASME-JSME-KSME Joint Fluids Engineering Conference*, Hamamatsu, 2011.

[22] M. Ahmadi-Baloutaki, R. Carriveau and D. S.-K. Ting, "Performance of a vertical axis wind turbine in grid generated turbulence," *Sustainable Energy Technologies and Assessments,* vol. 11, no. 1, pp. 178-185, 2015.

[23] E. Möllerström, F. Ottermo, A. Goude, S. Eriksson and J. Hylander, "Turbulence influence on wind energy extraction for a medium size vertical axis wind turbine," *Wind Energy,* vol. 157, no. 1, pp. 1-14, 2016.

[24] H. Y. Peng and H. F. Lam, "Turbulence effects on the wake characteristics and aerodynamic performance of a straight-bladed vertical axis wind turbine by wind tunnel tests and large eddy simulations," *Energy,* vol. 109, no. 1, pp. 557-568, 2016.

[25] A. C. Molina, T. Massai, F. Balduzzi, A. Bianchini, G. Ferrara, T. D. Troyer and G. Bartoli, "Combined experimental and numerical study on the near wake of a Darrieus VAWT under turbulent flows," in *Journal of Physics: Conference Series*, 2018.

[26] M. Andreu Carbo, T. D. Troyer, T. Massai, A. Vergaerde, M. C. Runacres and G. Bartoli, "Effect of turbulence on the performance of VAWTs: An experimental study in two different wind tunnels," *Journal of Wind Engineering & Industrial Aerodynamics,* vol. 192, no. 1, p. 103969, 2019.

[27] A. Sentchev, M. Thiébaut and F. G. Schmitt, "Impact of turbulence on power production by a free-stream tidal turbine in real sea conditions," *Renewable Energy,* vol. 147, no. 1, pp. 1932-1940, March 2020.

[28] M. Dhalwala, A. Bayram, P. Oshkai and A. Korobenko, "Performance and near-wake analysis of a vertical-axis hydrokinetic turbine under a turbulent inflow," *Ocean Engineering,* vol. 257, no. 1, p. 111703, 2022.

[29] T. C. Hohman, L. Martinelli and A. J. Smits, "The effects of inflow conditions on vertical axis wind turbine wake structure and performance," *Journal of Wind Engineering & Industrial Aerodynamics,* vol. 183, no. 1, pp. 1-18, 2018.

[30] R. E. Seoud and J. C. Vassilicos, "Dissipation and decay of fractal-generated turbulence," *Physics of Fluids,* vol. 19, no. 10, pp. 105-108, 2007.

[31] D. Xu and J. Chen, "Accurate estimate of turbulent dissipation rate using PIV data," *Experrimental Thermal and Fluid Science,* vol. 44, no. 1, pp. 662-672, 2012.

[32] P. Bachant and M. Wosnik, "Effects of Reynolds Number on the Energy Conversion and Near-Wake Dynamics of a High Solidity Vertical-Axis Cross-Flow Turbine," *Energies,* vol. 9, no. 2, p. 73, 2016.

[33] P. B. S. Lissaman, "Low-Reynolds-Number Airfoils," *Annual Review of Fluid Mechanics,* vol. 15, no. 1, pp. 223-239, 1983.

[34] B. H. Carmichael, "Low Reynolds Number Airfoil Survey," National Aeronautics and Space Administration, 1982.

[35] T. C. Yap, M. Z. Abdullah, Z. Husain, Z. M. Ripin and R. Ahmad, "The Effect of Turbulence Intensity on The Aerodynamic Performance of Airfoils," 2001.

[36] L. Damiola, M. F. Siddiqui, M. Runacres and T. De Troyer, "Influence of free-stream turbulence intensity on static and dynamic stall of a NACA 0018 aerofoil," *Journal of Wind Engineering and Industrial Aerodynamics,* vol. 232, no. 1, p. 105270, 2023.

[37] X. Huang, M. Albers, P. S. Meysonnat, M. Meinke and W. Schröder, "Analysis of the effect of freestream turbulence on dynamic stall of wind turbine blades," *International Journal of Heat and Fluid Flow,* vol. 85, no. 1, p. 108668, 2020.

[38] M. Boudreau and G. Dumas, "Comparison of the wake recovery of the axial-flow and cross-flow turbine concepts," *Journal of Wind Engineering and Industrial Aerodynamics,* vol. 165, no. 1, pp. 137-152, 2017.

[39] S. Zanforlin, "Effects of hydrofoil shape and turbine solidity on the wake energy recovery in cross-flow turbines," *Journal of Ocean Engineering and Marine Energy,* vol. 9, no. 1, pp. 547-566, 2023.

[40] L. Battisti, L. Zanne, S. Dell'Anna, V. Dossena, G. Persico and B. Paradiso, "Aerodynamic Measurements on a Vertical Axis Wind Turbine in a Large Scale Wind Tunnel," *Journal of Energy Resources Technology,* vol. 133, no. 3, p. 031201, 2011.

[41] H. C. Ghimire and S. C. C. Bailey, "An experimental investigation of wing-tip vortex decay in turbulence," *Physics of FLuids,* vol. 29, no. 1, p. 037108, 2017.

[42] K. B. Miloud, M. Dghim, H. Fellouah and M. Ferchichi, "Free-stream turbulence interaction with a wing-tip vortex," *Journal of Wind Engineering and Industrial Aerodynamics,* vol. 206, no. 1, p. 104211, 2020.

[43] D. Hurst and C. Vassilicos, "Scalings and decay of fractal-generated turbulence," *Physics of Fluids,* vol. 19, no. 1, p. 035103, 2007.

[44] A. Mahfouth, "Fractal Grid-Turbulence and its Effects on a Performance of a Model of a Hydrokinetic Turbine," University of Victoria, Victoria, 2008.

[45] T. S. Lee, E. H. Ooi, W. S. Chang and J. J. Foo, "Realisation of Fractal Grid-Induced Turbulence Strength with PTFV: Effects of Grid Geometry," *Flow, Turbulence and Combustion,* vol. 111, no. 4, pp. 1079-1099, 2023.

[46] A. Fuchs, W. Medjroubi, G. Guelker and J. Peinke, "Experimental and Computational Investigation of a Fractal Grid Wake," *arXiv:2210.06208,* 2022.

[47] R. Gomes-Fernandes, B. Ganapathisubramani and J. C. Vassilicos, "Particle image velocimetry study of fractalgenerated," *Journal of Fluid Mechanics,* vol. 711, no. 1, pp. 306-336, 2012.

[48] LaVision, "PIV Uncertainty Quantification," June 2018. [Online]. Available: https://www.lavision.de/en/download.php?id=2347&name=download.pdf. [Accessed 3 March 2022].

[49] H. Coleman and W. Steele, Experimentation, Validation, and Uncertainty Analysis for Engineers, 4rd ed., Hoboken: Wiley, 2018.

[50] International Organization for Standardization (ISO), "Guide to the Expression of Uncertainty in Measurement (GUM)," International Organization for Standardization (ISO), Geneva, 2008.

[51] A. Sentchev, M. Thiébaut and . F. G. Schmitt, "Impact of turbulence on power production by a free-stream tidal turbine in real sea conditions," *Renewable Energy,* vol. 147, pp. 1932-1940, 2020.

[52] A. Bouferrouk, J. P. Hardwick, A. M. Colucci and L. Johanning, "Quantifying turbulence from field measurements at a mixed low tidal energy site," *Renewable Energy,* vol. 87, no. 1, pp. 476-492, 2016.

[53] A. Choudhry, R. Leknys, M. Arjomandi and R. Kelso, "An insight into the dynamic stall lift characteristics," *Experimental Thermal and Fluid Science,* vol. 58, no. 1, pp. 188-208, 2014.

[54] G. L. Bretthorst, "Nonuniform Sampling: Bandwidth and aliasing," in *AIP*, 2001.

[55] G. S. Payne, T. Stallard, R. Martinez and T. Bruce, "Variation of loads on a three-bladed horizontal axis tidal turbine with frequency and blade position," *Journal of Fluids and Structures,* vol. 83, no. 1, pp. 156-170, 2018.

[56] H. C. Ghimire and S. C. C. Bailey, "An experimental investigation of wing-tip vortex decay in turbulence," *Physics of Fluids,* vol. 29, no. 3, p. 037108, 2017.

[57] M. Boudreau and G. Dumas, "Comparison of the wake recovery of the axial-flow and cross-flow turbine concepts," *Journal of Wind Engineering and Industrial Aerodynamics,* vol. 165, no. 1, pp. 137-152, 2017.

[58] K. B. Miloud, M. Dghim, H. Fellouah and M. Ferchichi, "Free-stream turbulence interaction with a wing-tip vortex," *Journal of Wind Engineering and Industrial Aerodynamics,* vol. 206, no. 1, p. 104211, 2020.

[59] L. C. Pagnini, M. Burlando and M. P. Repetto, "Experimental power curve of small-size wind turbines in turbulent urban enviorment," *Applied Energy,* vol. 154, no. 1, pp. 112-121, 2015.

[60] P. Bachant and M. Wosnik, "Characterising the near-wake of a cross-flow turbine," *Journal of Turbulence,* vol. 16, no. 4, pp. 392-410, 2015.

[61] S. Wang, Y. Zhou, M. M. Alam and H. Yang, "Turbulent intensity and Reynolds number effects on an airfoil at low Reynolds numbers," *Physics of Fluids,* vol. 26, no. 1, p. 115107, 2014.

[62] Y. Yang, Z. Guo, Y. Zhang, H. Jinyama and Q. Li, "Numerical Investigation of the Tip Vortex of a Straight-Bladed Vertical AxisWind Turbine with Double-Blades," *Energies,* vol. 10, no. 1, p. 11, 2017.

Appendix A: Turbulence Grid Design

Square space-filling fractal grids were employed in Chapter 2: to subject the cross-flow turbine to intermediate and high turbulence inflow levels, representing approximately 5% and 10% turbulence intensity, respectively. These fractal grids were selected due to their ability to produce higher turbulence levels at a lower blockage level relative to conventional bar grids [30]. The geometry of square space-filling fractal grids is generated through repetitive recursion of hollow squares with specific bar lengths and bar thicknesses at each iteration. The total number of grid iterations is denoted by the fractal number, N_f, where the jth iteration denotes the individual recursion level. The associated iteration bar length and bar thickness are defined by L_{j-1} and t_{j-1}, respectively. A length scaling factor, $R_L = L_j/L_{j-1}$, and a thickness scaling factor, $R_t = t_j/t_{j-1}$, reduces successive iterations [43]. With the five variables introduced and defined: L_0, t_0, R_L, R_t, and N_f, the square space-filling fractal grid is fully defined.

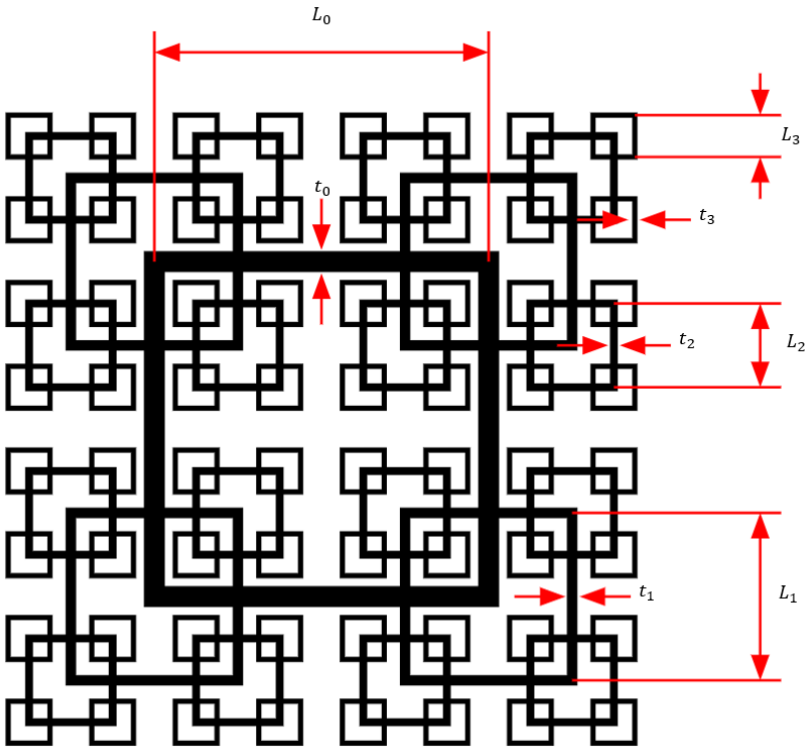

Figure A1: Example of a four-iteration (N_f = 4) square space-filling fractal grid. The bar lengths of: L_0, L_1, L_2, L_3 and the bar thicknesses of t_0, t_1, t_2, t_3 corresponds to the 1st, 2nd, 3rd, and 4th grid iterations, respectively.

These five variables, L_0, t_0, R_L, R_t, and N_f, can be used to further constrain the design by applying variable relationships established within the literature and physical limits from the experimental system. Experimental work has shown that a length scaling ratio of $R_L = 1/2$ produces the most homogeneous turbulence [43], thereby fixing the length ratio between grid iterations. Additionally, the fractal grid was designed to fill the entire width of the water channel, controlling the bar lengths. This constraint can be applied to the grids, allowing for the following relationship:

$$L_0 = \frac{T - t_{N_f - 1}}{\sum_{j=1}^{N_f} \left(\frac{1}{2}\right)^{j-1}} \ , \tag{A1}$$

where T is the width of the water flume. The next variable that can be constrained is the fractal number. A four-iteration (N_f = 4) grid was selected as it produces more homogeneous, isentropic turbulence compared to grids with a lower fractal number [43]. The last constraint introduced establishes a relationship between the thickness scaling factor and the first iteration bar thickness; this is the blockage ratio of the grid. The grid blockage ratio, σ, is defined by the area occupied by the grid compared to the cross-section area of the tunnel, defined by:

$$\sigma = \frac{L_0 t_0 \sum_{j=0}^{N_f - 1} 4^{j+1} R_L^j R_t^j - t_0^2 \sum_{j=1}^{N_f - 1} 2^{2j+1} R_t^{2j-1}}{T^2} \ . \tag{A2}$$

Where T^2 is the cross-sectional area of the water channel. A common blockage ratio of 25% is observed throughout the literature [43], [44], as it provides a balance between turbulence generation and homogeneity [45]. At this point, the only variables left unconstrained are t_0 and R_t, which are related through the thickness scaling ratio and Eqn. (2). Equating these two equations facilitates control over the grid design using a single unconstrained design variable. This method of creating a dependency across variables is similar to Hurst and Vassilicos [43], where they design various grids based on one parameter referred to as the thickness ratio given by the relationship $t_r = R_t^{1-N_f}$.

Turbulent statistics are typically taken at the centerline of the fractal grids [45]; however, the objective here is to characterize the average turbulence properties within the projected area

upstream of the turbine. To guide the grid design, experimental studies by Mahfouth [44], Fuchs et al. [46], and Gomes et al. [47] were referenced, as all employed PIV to visualize flow field characteristics across the midspan of the grid. These studies reveal that off centerline turbulence intensities tend to increase due to a slight reduction in streamwise velocity. Based on the results from Gomes et al. [47], a thickness ratio of 13 was chosen as it corresponds to an approximately 11% average centerline turbulence intensity, making this a suitable candidate for the high turbulence design case. Designing for a slightly higher than intended turbulence intensity is desirable as the turbine is expected to decelerate the streamwise flow as it approaches the turbine.

To define the intermediate case, the relationship $u'^2_{peak} \propto t_r$, established by Hurst and Vassilicos [43], is used. Applying this scaling relationship and the target thickness ratio for the high turbulence design case, a corresponding thickness ratio of 3.25 is derived to achieve the target turbulence intensity of 5% for the intermediate case. Thus, the two target design cases are fully defined: an Intermediate turbulence case targeting 5% turbulence intensity with a thickness ratio of 3.25 and a high turbulence case targeting 10% turbulence intensity with a thickness ratio of 13.

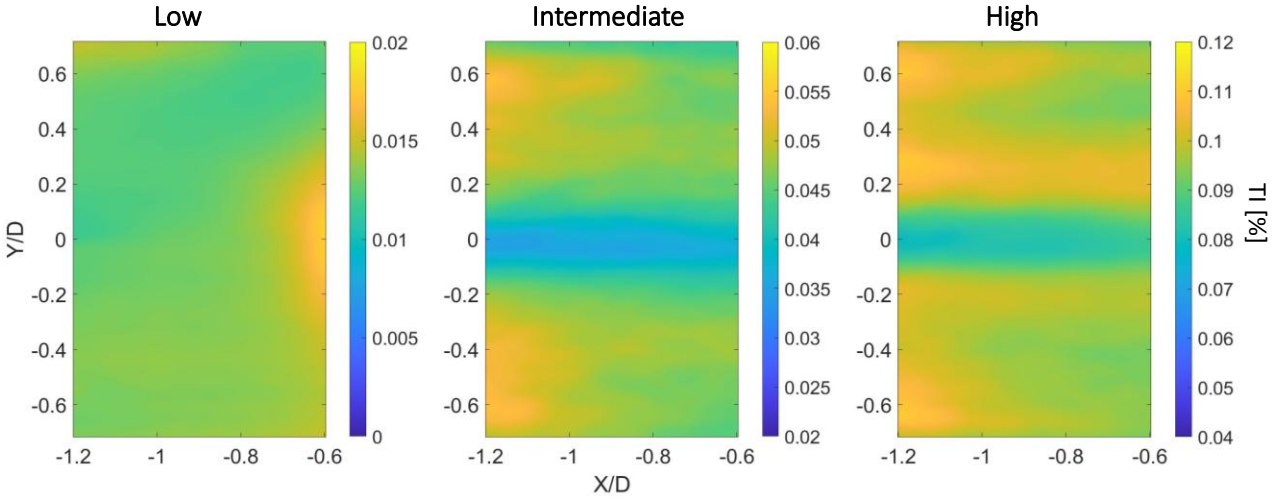

Figure A2: PIV results of the turbulent inflow in front of the turbine for the three turbulence intervals: baseline TI = 1.4%, intermediate TI = 4.7%, and high TI = 10.6%. The rotor axis is located at X/D = 0.

The turbulence intensity of each of the three turbulent intervals was calculated by averaging seven points upstream of the turbine, at a radius of 0.75D from turbine's origin, spanning from $-0.6 \leq Y/D \leq 0.6$. The average Streamwise turbulence intensity values are shown in Figure A2, where the baseline, intermediate, and high turbulence cases produced turbulence magnitude values of $1.4 \pm 0.2\%$, $4.7 \pm 0.5\%$, and $10.6 \pm 0.8\%$, respectively.

Appendix B: Uncertainty Analysis

The two main types of uncertainty were considered throughout the experimental campaign: systematic and random. For the performance data, the associated systemic error was obtained from sensor calibration or the equipment data sheet's uncertainty value. The random error was quantified from the standard deviation of the instantaneous rotor torque. For the velocity data, systematic and random errors were obtained from a built-in processing tool within the PIV software, Davis 10.0.2, which applies a correlation statistics method to estimate these uncertainties [48]. The 95% uncertainty confidence interval was computed for C_p, mean inflow, and wake velocities by using:

$$U_{95} = z_{95} u_x \ , \tag{B1}$$

where $z_{95}\ (= 1.96)$ corresponds to the z-distribution value for a 95% confidence interval, and u_x is the combined systematic and random uncertainty, calculated from [49]:

$$u_x^2 = \ s_x^2 + \ b_x^2 \ . \tag{B2}$$

Where s_x is the standard deviation from the mean turbine rotation, associated with random error, and b_x is the systematic uncertainty. The systematic uncertainty was calculated using a root sum squares method, as follows [50]:

$$b_X^2 = \sum_{i=1}^{j} \left(\frac{\partial X}{\partial x_i}\right)^2 b_{x_i}^2 \ \ , \tag{B3}$$

where x_i is the primitive quantity used to calculate the desired result X (e.g. C_P, U_x, U_y, etc.), and $b_{x_i}$is the systematic uncertainty, projected as half the least count listed on the equipment's manufacturer documentation.

Table B1: Average combined standard uncertainty for the power coefficient, inflow velocity, and wake velocity for each of the three turbulent inflow cases. The free-stream velocity is 1.6 m/s in all cases.

Turbulence Case	C_p	Inflow		Wake	
		X-Velocity (m/s)	Y-Velocity (m/s)	X-Velocity (m/s)	Y-Velocity (m/s)
Baseline	0.005	0.031	0.030	0.058	0.059
Intermediate	0.008	0.046	0.044	0.062	0.060
High	0.009	0.050	0.049	0.065	0.064

Table B1 displays the average combined uncertainty for the power coefficient, the inflow velocity field, and the wake velocity field. The C_p at lower TSRs experience uncertainty dominated by the systematic error from the torque transducer; the higher the TSR, the less affected the measurements were. At TSR = 2.65, the uncertainty for the three turbulence levels was: 3.3% for the low turbulence case, 7.2% for the intermediate turbulence case, and 4.8 % for the high turbulence case. As for the wake uncertainty, the uncertainty was significantly higher directly behind the turbine, resulting in an error of nearly 5% in the velocity for all three turbulence cases, dropping to <2% by 6 diameters downstream from the turbine.